Photonics-Based MIMO Radar With Broadband Digital Coincidence Imaging

Guanqun Sun, Yuewen Zhou, Yuhui He, *Student Member, IEEE*, Xiaoyue Yu, Fangzheng Zhang, *Senior Member, IEEE*, and Shilong Pan, *Fellow, IEEE*

***Abstract*— Photonics-based radars with a large operation bandwidth enable a high-range resolution. Achieving high angular resolution typically demands a large aperture size or a large antenna array, causing increased system complexity, volume, and cost. In this article, we propose a photonics-based multiple-input and multiple-output (MIMO) radar that employs a broadband digital coincidence imaging (DCI) method to achieve super-resolution radar imaging. In the proposed radar system, period one (P1) laser dynamics is used to generate broadband linear frequency modulation (LFM) signals, and photonic frequency mixing is adopted to implement de-chirp processing. To improve the angular resolution, the proposed DCI method implements random phase modulation and multichannel accumulation to the photonic de-chirped signals in the digital domain, obtaining radar observation samples with rich spatiotemporal diversity. Based on the spatiotemporally incoherent observation process, an imaging equation is constructed and solved by a sparse reconstruction method, resulting in the final high-resolution radar image. A photonics-based 8 × 8 MIMO radar with a bandwidth of 8 GHz (18–26 GHz) is established. Applying the proposed DCI method, super-resolution 3-D imaging is successfully demonstrated, attaining a range resolution of 2 cm, an azimuth resolution of 0.3°, and an elevation resolution of 0.3°. The experimental results can soundly verify that the proposed photonics-based MIMO radar provides a promising solution to high-resolution forward-looking radar imaging.**

***Index Terms*— Coincidence imaging, microwave photonics, multiple-input and multiple-output (MIMO), radar.**

I. Introduction

With the continuous development of signal processing theory and hardware processing capability, radar imaging has evolved into a fundamental function of radar systems. Thanks to the features of all-weather, all-time, and long-distance observation, radar imaging has been widely used in celestial mapping, space debris monitoring, topographic mapping, ocean observation, etc. [1], [2]. In recent years, photonic technologies have been applied in radar systems to expand the operation bandwidth for both radar signal generation and reception, particularly sharpening the range resolution in radar systems [3], [4], [5], [6], [7], [8], [9], [10], [11], [12]. Up to now, several photonics-based synthetic aperture radars (SARs) and inverse SARs have been developed for high-resolution imaging [13], [14], [15], [16], [17], [18], [19], [20], [21], with demonstrated range resolutions reaching up to 8.3 mm [21]. However, achieving high azimuth resolution typically necessitates extended observation periods to form a large equivalent aperture size, which will reduce processing speed and pose challenges in imaging fast-moving targets. Additionally, SARs and ISARs are constrained by the necessity of relative motion between radar and target, restricting their operation to side or squint-looking imaging modes [22], [23]. To expand the visual field, forward-looking imaging using array radars can be applied. However, attaining a high angular resolution requires a large-size array and a large number of transmit and receive channels. Multiple-input and multiple-output (MIMO) radars offer an efficient approach for emulating large array structures using fewer transmit and receive elements [24], [25], [26], [27]. Specifically, an array comprising M transmitters and N receivers, denoted as an $M \times N$ MIMO setup, effectively mirrors the capabilities of a single array with a total of MN elements. To improve the range resolution of conventional MIMO radars, photonics-based MIMO radars have been proposed [28], [29], [30], [31], [32], [33], [34]. These radar systems employ different microwave photonic technologies for the generation and processing of broadband linear frequency modulation (LFM) signals. For example, in [32], a photonics-based frequency-division multiplexing (FDM) MIMO radar is proposed in which optical frequency combs heterodyning is applied to generate multiple LFM signals in different frequency bands and photonic frequency mixing is applied to perform de-chirping processing in the multiple receivers. Based on this MIMO radar, high-resolution imaging with a back projection (BP) algorithm is achieved. In [33], a photonics-based time-division multiplexing (TDM) MIMO radar using photonic frequency multiplication for broadband LFM signal generation is proposed, through which high resolution imaging of complex targets is implemented using a modified broadband BP imaging algorithm. In [34], a photonics-based TDM-MIMO radar using photonic digital-to-analog conversion for LFM signal generation is proposed, and field-trial 3-D imaging of a civil aviation aircraft is demonstrated. For these photonics-based MIMO radars, although the angular resolution is improved

Manuscript received 1 April 2024; revised 15 May 2024; accepted 4 June 2024. Date of publication 18 June 2024; date of current version 5 December 2024. This work was supported in part by the National Key Research and Development Program of China under Grant 2021YFB2800803, in part by the Natural Science Foundation of China under Grant 62371224, in part by the Natural Science Foundation of Jiangsu Province under Grant BK20221479, in part by the Fundamental Research Funds for the Central Universities under Grant NS2023023, and in part by the Fund of Prospective Layout of Scientific Research for NUAA. *(Corresponding author: Fangzheng Zhang.)*

The authors are with the National Key Laboratory of Microwave Photonics, Nanjing University of Aeronautics and Astronautics, Nanjing 210016, China (e-mail: zhangfangzheng@nuaa.edu.cn).

Color versions of one or more figures in this article are available at https://doi.org/10.1109/TMTT.2024.3411120.

Digital Object Identifier 10.1109/TMTT.2024.3411120

compared with ordinary array radars, it is still constrained by the Rayleigh limit. Therefore, to achieve high angular resolution, the transceiver array needs to have a large size, which is difficult to achieve in practical applications.

In this article, we propose a photonics-based MIMO radar with super-resolution imaging capability by using a digital coincidence imaging (DCI) method. In the proposed system, an optical injection semiconductor laser is used to generate broadband LFM signals, and photonic frequency mixing is applied to realize de-chirp processing of the broadband radar echoes. The proposed MIMO radar works in TDM manner which allows a single radar transmitter for generating multichannel orthogonal signals and a single radar receiver for efficiently capturing the multichannel radar echoes without aliasing. Thanks to the microwave photonic signal generation and processing, the radar transceivers can operate in a large bandwidth, leading to a high range resolution. Besides, the implementation of TDM mechanism optimizes spectral efficiency, facilitating broad operation bandwidths within each channel. Moreover, the TDM mechanism maintains channel orthogonality and affords considerable adaptability in configuring numerous transmit and receive channels. To break through the Rayleigh resolution limit, a DCI method is proposed in which the de-chirped signals are randomly modulated in the digital domain. This imaging method increases the temporal-spatial diversity of the observing signals, and hence enables super-resolution imaging in both azimuth and elevation directions. To achieve accurate image construction and interference suppression, based on the spatiotemporally incoherent observation process, sparse reconstruction method is applied to solve the constructed imaging equation. In the experiment, a photonics-based 8 × 8 MIMO radar is constructed with a bandwidth of 8 GHz (18–26 GHz), of which the range resolution reaches 2 cm. Utilizing this radar system and the proposed DCI method, broadband forward-looking imaging is demonstrated and analyzed. The results verify the superior performance of the proposed photonics-based MIMO radar, which outperforms the traditional MIMO radars with six times higher resolution in both azimuth and elevation directions.

The subsequent sections of this article are structured as follows. Section II introduces the principle of the proposed photonics-based MIMO radar. In Section III, the design of the photonics-based broadband 8 × 8 MIMO radar system is discussed and super-resolution imaging is demonstrated. Finally, Section IV draws conclusions.

II. Principle

In this section, the principle of the photonics-based radar transceiver is first presented, which is the basis for constructing the MIMO radar. Then, the photonics-based MIMO radar system is introduced and the principle of DCI based on the proposed MIMO radar is expatiated.

A. Photonics-Based Radar Transceiver

Fig. 1 shows the structure of the photonics-based radar transceiver. It utilizes period-one (P1) oscillation in an optically injected semiconductor laser to generate broadband

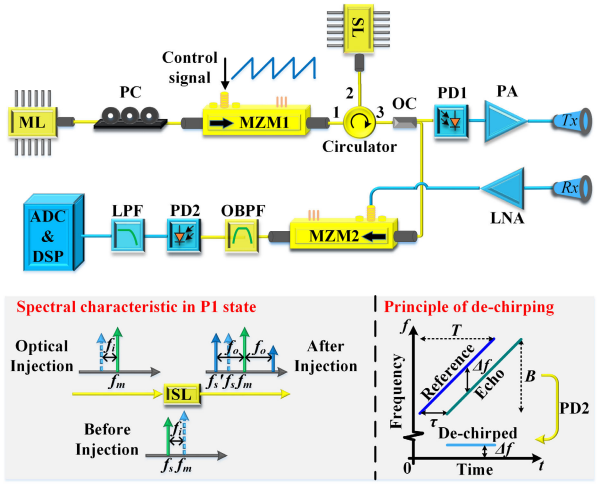

Fig. 1. Schematic of the photonics-based radar transceiver.

LFM signals [35]. De-chirp processing of the radar echoes is achieved through photonic frequency mixing, with the optical signal in the lower branch of the optical coupler (OC) serving as the reference. Radar echoes collected by the receive antenna (Rx) undergo amplification by a low noise amplifier (LNA) before being fed into the Mach-Zehnder modulator (MZM2). After modulating the regenerated optical carrier in the reference optical signal, a new frequency-swept optical sideband will be generated. This newly generated frequency-swept sideband together with the frequency-swept sideband of the reference optical signal is filtered out by an optical bandpass filter (OBPF). Subsequently, the obtained optical signal is sent to a photodetector (PD2) for photonic frequency mixing, which performs de-chirping of the radar echo [15]. After PD2, an electrical low-pass filter (LPF) is used to select the de-chirped signal, eliminating high-frequency disruptions. This filtered signal is then digitized by an analog-to-digital converter (ADC) and further processed within a digital signal processing (DSP) module.

For the proposed radar transmitter, thanks to the dominance of P1 oscillation within the state space of the optically injected semiconductor laser, the generated LFM signals can have a very large bandwidth. The central frequency, bandwidth, and pulsewidth of these signals can be easily adjusted by properly setting the optical injection parameters [35], [36]. Moreover, the generated LFM signals exhibit characteristics such as LFM, high in-band signal-to-noise ratio (SNR), and good phase coherence, as verified in previous demonstrations [37], [38], [39], [40], [41], [42], [43]. In the receiver, the microwave photonic frequency mixing has good consistency over a very large operation bandwidth and enables broadband de-chirp processing with a highly spurious-free dynamic range [44]. Additionally, the optical connection between transmitter and receiver contributes to system compactness and stability. Therefore, the photonics-based radar transceiver has the advantages of both large bandwidth and high-performance, which helps to achieve high range resolution detection and imaging.

B. TDM-MIMO Radar With DCI

Fig. 2 shows the schematic of the photonics-based MIMO radar, which contains M transmit channels and N receive

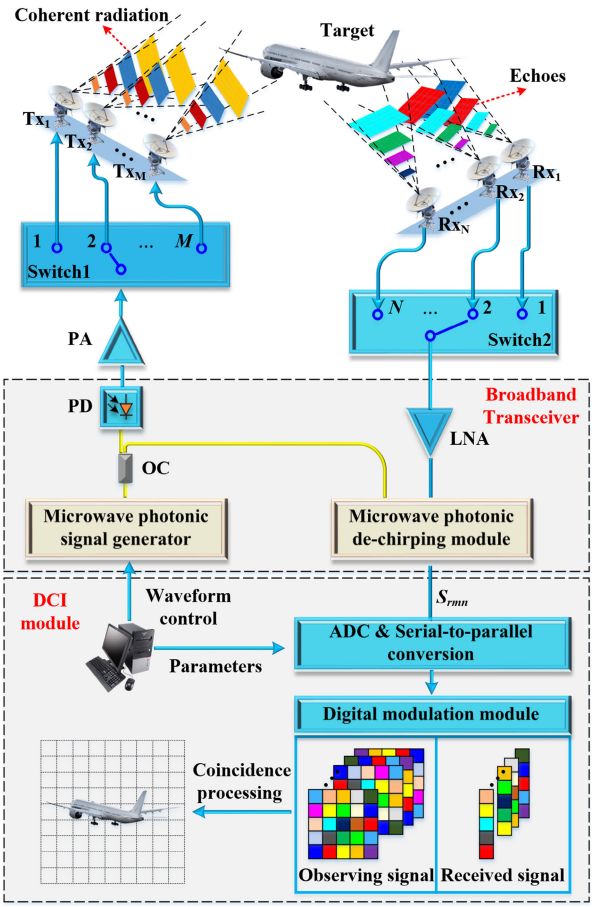

Fig. 2. Schematic of the photonics-based MIMO radar utilizing DCI method.

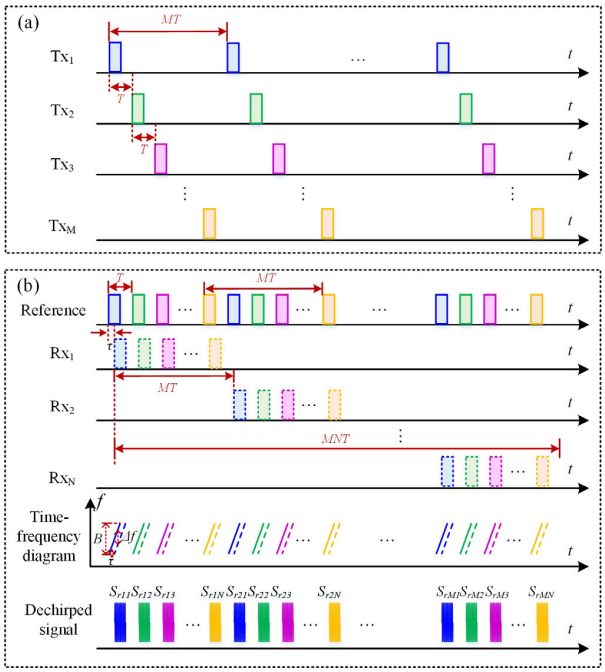

Fig. 3. Temporal sequence of (a) transmit channels and (b) receive channels.

channels. The principle of the microwave photonic signal generator is the same as the optical injection part in Fig. 1. The output optical signal from the slave laser (SL) is split into two branches by an OC. In one branch, the signal is directed to a PD to generate a broadband LFM signal, which is amplified by a power amplifier (PA) and fed into a $1 \times M$ RF switch (Switch1). Switch1 is properly controlled to let every M radar pulse be sequentially output to the M transmit channels. This way, the M-channel LFM signals are emitted to the detection area through M transmit antennas in a TDM manner. Fig. 3(a) shows the temporal sequence of the M transmit channels, in which T is the temporal period of the generated LFM signal.

In the receiver, the radar echoes received by the N receive antennas are directed to an $N \times 1$ RF switch (Switch2). Switch2 alternates the enabling channel at intervals of MT, allowing each channel to receive echoes from all the M transmit channels in a TDM manner. After N times of switches, the radar echoes corresponding to all the MN transmit-receive channels are sequentially allocated in different time slots. So far, the transmit and receive process of a single MIMO detection period is completed, which takes a total time of MNT. The received echoes are amplified by a LNA and fed into a microwave photonic de-chirping module. Concurrently, the signal from the other branch of the OC is directed into the microwave photonic de-chirping module, serving as the optical reference for de-chirp processing. The fundamental de-chirping principle is similar to that in Fig. 1, with the distinction that the de-chirping of radar echoes corresponding to different transmit-receive channels is executed in a TDM manner, as shown in Fig. 3(b). By performing serial-to-parallel conversion, the de-chirped signals, which are sampled by the ADC within a single MIMO detection period, are separated into MN segments based on the temporal sequence. Each segment is then mapped in sequence to a distinct transmit-receive channel. This way, a received signal matrix $\mathbf{S}_r$ consisting of MN de-chirped signals can be obtained, in which the element $S_{rmn}(t)$ $(m = 1, 2, 3, \ldots, M;\ n = 1, 2, 3, \ldots, N)$ corresponds to the mth transmit channel and the nth receive channel. Based on the received signal matrix and the steering vector matrix of the MIMO radar array, radar imaging is generally realized by the digital beamforming (DBF) method in traditional systems, whereas the angle resolution is still limited by the size of the radar array.

To break through the Rayleigh limit and implement super-resolution forward-looking imaging, a DCI method is proposed and applied to process the received signals, the basic principle of which is illustrated in Fig. 2. By modulating the received signal in the digital domain, a spatiotemporal incoherent observation process is formed in the imaging area. The scattering centers of the target within a beam will reflect and enable the radar to obtain different observing signals based on their respective positions, thereby achieving super-resolution within the beam. Specifically, first, a parametric imaging model is formulated based on the system parameters and the transmit-receive processes. The imaging area is divided into K grid units of the same size, and a collection of discrete imaging units is obtained as

$$I = \{\mathbf{r}_1, \mathbf{r}_2, \ldots, \mathbf{r}_K\} \tag{1}$$

where $\mathbf{r}_k$ is the center position vector of the kth imaging unit. Assuming the scattering points of the target are located in the center of the imaging units, the scattering coefficient vector of

the target can be expressed as

$$\boldsymbol{\sigma} = [\sigma_1, \sigma_2, \ldots, \sigma_K]^T \tag{2}$$

where σ_k represents the scattering coefficient of the kth imaging unit. Thus, the received signal corresponding to the mth transmit channel and nth receive channel is

$$S_{rmn}(t) = \sum_{k=1}^{K} \sigma_k \cdot S_{tm}\left(t - \tau_{mn}^k\right). \tag{3}$$

In (3), $S_{tm}(t)$ is the LFM signal emitted by the mth transmit antenna and τ_{mn}^k is the time delay of this signal reaching the kth imaging unit and reflected to the nth receive antenna

$$\tau_{mn}^k = \frac{1}{c}\left(\left\|\mathbf{r}_k - \mathbf{R}_{t,m}\right\| + \left\|\mathbf{r}_k - \mathbf{R}_{r,n}\right\|\right) \tag{4}$$

where $\mathbf{R}_{t,m}$ and $\mathbf{R}_{r,n}$ represent the position vectors of the mth transmit antenna and the nth receive antenna, respectively, and c is the propagation speed of the electromagnetic wave in the atmosphere.

Then, to make the observation process have more spatiotemporally incoherent differences and meet the restricted isometry property (RIP), a random phase modulation is applied to the received signals of each transmit-receive channel in the digital domain. Subsequently, the phase-modulated signals are summed up to get

$$S_r'(t) = \sum_{m=1}^{M}\sum_{n=1}^{N} S_{rmn}(t) \cdot \exp\left[j \cdot W_{mn}(t)\right] \tag{5}$$

where $W_{mn}(t)$ represents the random phase modulation term corresponding to the mth transmit channel and the nth receive channel. Similarly, the observing signal of the imaging area can be derived from the observation process and the geometric relationship

$$S(t, \mathbf{r}_k) = \sum_{m=1}^{M}\sum_{n=1}^{N} S_{tm}\left(t - \tau_{mn}^k\right) \cdot \exp\left[j \cdot W_{mn}(t)\right]. \tag{6}$$

It is deduced from (5) and (6) that the phase-modulated signal can be expressed as

$$S_r'(t) = \sum_{k=1}^{K} \sigma_k \cdot S(t, \mathbf{r}_k). \tag{7}$$

Subsequently, a parameterized imaging model can be obtained through discrete sampling

$$\mathbf{S}_r' = \mathbf{S} \cdot \boldsymbol{\sigma} \tag{8}$$

where $\mathbf{S}_r'$ is the modulated and summed received signal matrix. $\mathbf{S}$ is the observation matrix of the proposed photonics-based MIMO radar for the divided imaging area, which is formed by the observing signals at different grid-unit centers. Equation (8) can be expanded as

$$\begin{bmatrix} S_r'(t_1) \\ S_r'(t_2) \\ \vdots \\ S_r'(t_L) \end{bmatrix} = \begin{bmatrix} S(t_1, \mathbf{r}_1) & S(t_1, \mathbf{r}_2) & \cdots & S(t_1, \mathbf{r}_K) \\ S(t_2, \mathbf{r}_1) & S(t_2, \mathbf{r}_2) & \cdots & S(t_2, \mathbf{r}_K) \\ \vdots & \vdots & & \vdots \\ S(t_L, \mathbf{r}_1) & S(t_L, \mathbf{r}_2) & \cdots & S(t_L, \mathbf{r}_K) \end{bmatrix} \cdot \begin{bmatrix} \sigma_1 \\ \sigma_2 \\ \vdots \\ \sigma_K \end{bmatrix} \tag{9}$$

in which $t_1, t_2, \ldots, t_L$ are different sampling times. Now, the image reconstruction becomes the problem of solving (9). When the matrix $\mathbf{S}$ is nonsingular, the scattering coefficient of the target can be uniquely solved. The column vector and row vector of $\mathbf{S}$ represent the observing signals at different imaging units and different sample times, respectively. Therefore, the obvious spatiotemporal incoherence of the observation matrix ensures that the scattering coefficient of the target can be uniquely solved to realize super-resolution imaging.

The matched filtering method and pseudo-inverse method are commonly used methods for solving the imaging equation in (9), which can directly retrieve the scattering coefficient σ from $\mathbf{S}_r'$. However, because of the incomplete spatiotemporal incoherence of the observation matrix, image construction with these methods has limited super-resolution factor and suffers from sidelobe and background interferences. To get high-quality super-resolution images, compressed sensing method can be applied. It can be seen from (9) that the imaging equation to be solved is naturally consistent with the sparse reconstruction model. Based on the scattering center model, the backscattering of the radar target can be approximated as coming from a few strong scattering centers. Therefore, it is usually assumed that the number of scatterers is much less than the imaging grid units, i.e., the target to be reconstructed has the characteristic of spatial sparsity. Using the sparse prior condition of scattering coefficients, the compressed sensing algorithm can be employed to estimate the scattering coefficients σ even if the effective measurement data is insufficient [45], [46], [47], [48]. In addition, it can overcome the defects of the wide main-lobe and high-energy sidelobes in traditional methods, improving the performance of radar imaging. Based on this, the sparse constraint is added to the imaging equation of (8), which is obtained as follows:

$$\hat{\boldsymbol{\sigma}} = \arg\min_{\boldsymbol{\sigma}}\left\{\left\|\mathbf{S}_r' - \mathbf{S} \cdot \boldsymbol{\sigma}\right\|_2^2 + \lambda\left\|\boldsymbol{\sigma}\right\|_1\right\} \tag{10}$$

where λ is the regularization parameter. The greedy algorithms or convex optimization methods can be used to solve (10) and high-quality super-resolution imaging can be achieved.

It should be noted that to reduce the system complexity and save the cost, TDM manner is adopted in the photonics-based MIMO radar transceiver. Because of the inherent inferiority of TDM radars in detecting high-speed targets, the proposed radar is suitable for high-resolution imaging of slow-moving or stationary targets. While the proposed DCI method is not confined to TDM-MIMO radars. It can be applied in various array radars to enhance the imaging resolution.

III. Experiments and Results

In the conducted experiment, a photonics-based broadband 8 × 8 MIMO radar is established, as shown in Fig. 4(a). To control the optical injection intensity, the optical signal from the master laser (ML, TeraXion PS-TNL) is input to a 10-Gb/s MZM (MZM1, Lucent 2623NA) after passing through a PC. Subsequently, the modulated signal is directed into an SL (Actech LD15DM) via a circulator. MZM1 is driven by an electrical control signal generated by a low-speed electrical signal generator (RIGOL DG4062). The bias current of the

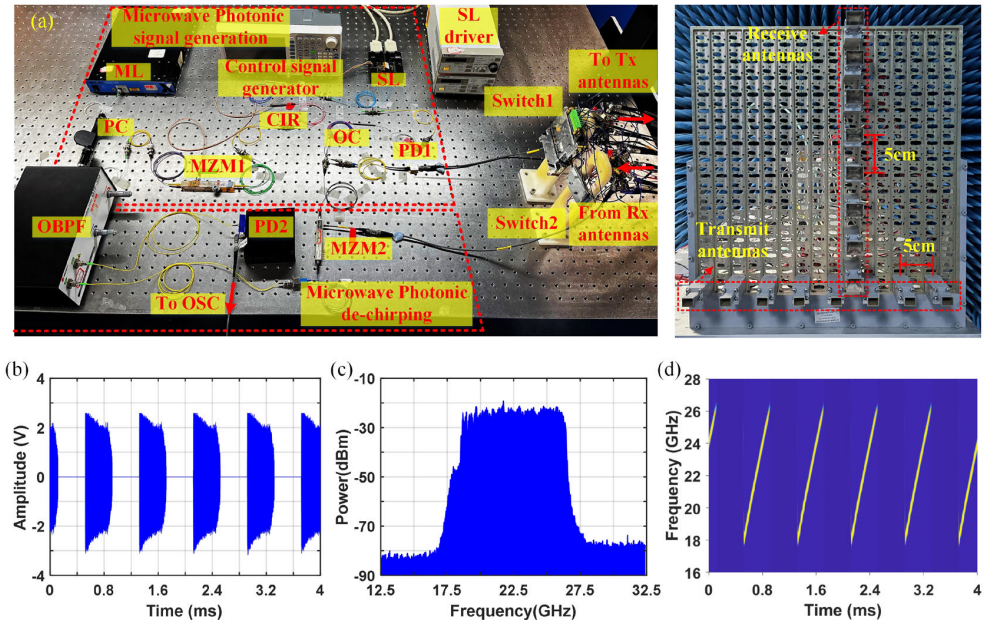

Fig. 4. (a) Photograph of the established photonics-based MIMO radar. (b) Temporal waveforms. (c) Electrical spectrum. (d) Time-frequency diagram of the generated LFM signals.

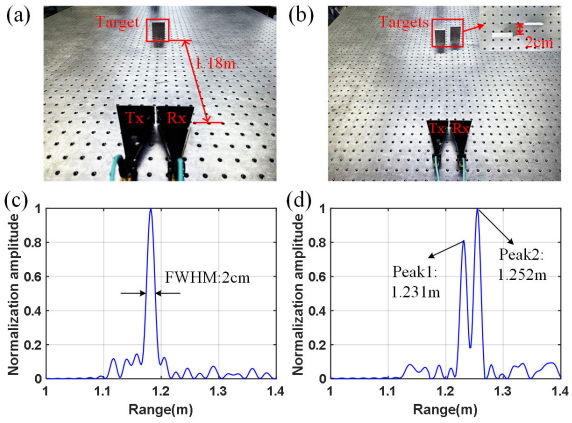

Fig. 5. Picture of (a) single-target detection scenario and (b) dual-target detection scenario. The range profile of (c) single-target detection and (d) dual-target detection.

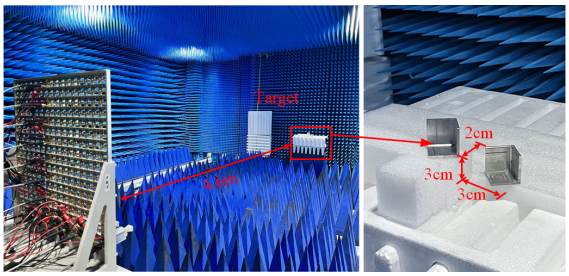

Fig. 6. Photograph of the 3-D imaging scenario with two corner reflectors separated by 0.02 m, 0.03 m (0.3°), and 0.03 m (0.3°) in range direction, azimuth direction, and elevation direction.

SL is adjusted to 24.4 mA, approximately four times of its threshold current. At the output of PD1 (u2t XPDV2120RA; bandwidth: 40 GHz), an LFM signal is generated and amplified by a PA (Operation bandwidth: 2–43 GHz; gain: 42 dB; maximum RF input power: +15 dBm; noise figure: 4 dB). The waveform analysis of the generated signal is performed using a real-time oscilloscope (Keysight DSO-X 93 204 A). Its temporal waveform and electrical spectra are depicted in Fig. 4(b) and (c), respectively. Fig. 4(d) depicts the instantaneous frequency characteristics of the generated signal calculated by short-time Fourier transform. It is observed that an LFM signal is successfully generated with a bandwidth of 8 GHz (18–26 GHz). The LFM signal exhibits a pulsewidth of 400 μs and a duty cycle of 50%. The generated signal is then directed to eight channels utilizing a single-pole eight-throw switch (Talent Microwave Inc. TLSP8T8G26), where the switching time between adjacent transmit channels is set at 800 μs. Subsequently, eight horn antennas (Tx, 18–26.5 GHz), positioned at 5 cm intervals in the azimuth direction, are used to transmit the microwave signals to the imaging area.

In the receiver, eight antennas are configured as a uniform linear array (ULA) oriented perpendicular to the transmit array to collect the radar echoes. The spacing between adjacent receive antennas is 5 cm. The established MIMO array has baseline lengths of 35 cm in both azimuth and elevation directions. Another single-pole eight-throw switch (Talent Microwave Inc. TLSP8T8G26) having a switching time of 6.4 ms between different channels is employed to combine the radar echoes of different transmit channels into one channel. According to the array size and the signal parameters, the established photonics-based MIMO radar takes 51.2 ms for a single round of transmission and reception for all 64 transmit-receive channels. The combined echoes are amplified by an LNA (Operation bandwidth: 18–26.5 GHz; gain: 35 dB; maximum RF input power: +10 dBm; noise figure: 1.8 dB) and connected to the RF port of MZM2 (Fujitsu FTM7938) to modulate the optical carrier. The subsequent selection of the desired optical modulation sidebands is achieved using an (OBPF, Santec: OTF-350). Next, another PD (PD2, CONQUER Inc; Bandwidth: 10 GHz) is used to complete the photonic frequency mixing and an LPF having a bandwidth of 200 MHz is applied to select out the de-chirped signal. Then the de-chirped signals are sampled and recorded by an electrical ADC with a sampling rate of 6.25 MSa/s. The radar

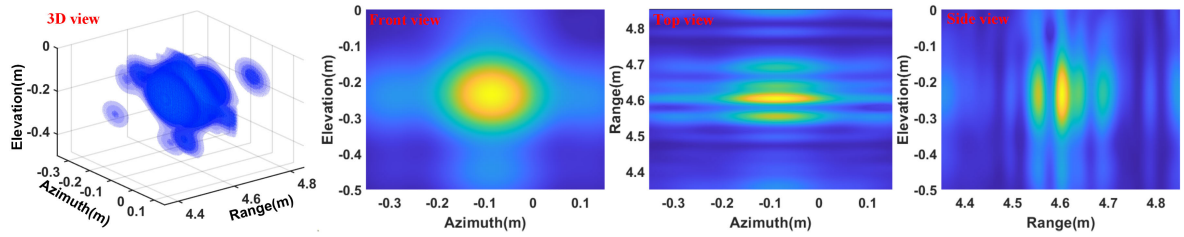

Fig. 7. Reconstructed images of two corner reflectors using DBF method.

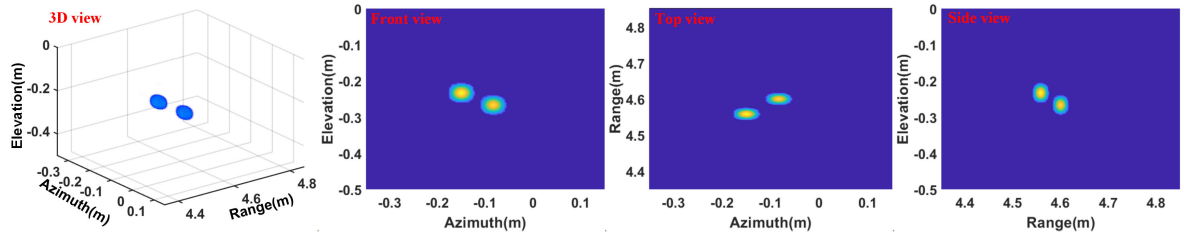

Fig. 8. Super-resolution imaging result of two corner reflectors obtained by the proposed DCI method.

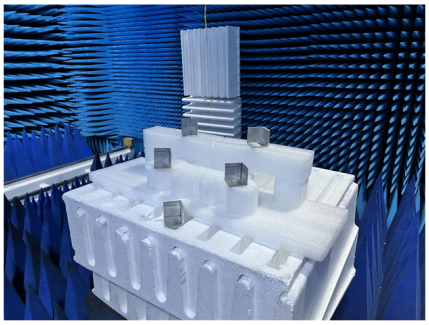

Fig. 9. Photograph of the 3-D imaging scenario of a U-shaped complex target.

parameters lead to a maximum unambiguous detection range of 23.42 m, which is sufficient in our experimental demonstrations. In practical applications, long distance detection can be achieved by adjusting the parameters of the photonics-based radar transceiver.

To investigate the range resolution of radar detection using the generated broadband signals, a ranging experiment is carried out. As shown in Fig. 5(a), the broadband LFM signals generated by the transmitter is directly emitted using a K-band horn antenna (Tx, 18-26.5 GHz) for detection. Another horn antenna (Rx, 18–26.5 GHz) is employed to receive the echoes, which are then transmitted to the receiver. First, a reflector positioned at 1.18 m away from the radar transceiver serves as the target. Utilizing a fast Fourier transformation (FFT) on the de-chirped signal, the range profile is obtained, as depicted in Fig. 5(c), in which a dominant peak appears at the position corresponding to the distance of the target. The full width at half maximum (FWHM) of the peak pulse in Fig. 5(c) is 2 cm, closely matching the theoretical range resolution of 1.875 cm. To further test the range resolution, detection of two closely spaced targets is conducted, as illustrated in Fig. 5(b), in which the two reflectors are separated by 2 cm along the range direction. In the range profile depicted in Fig. 5(d), two discernible peaks corresponding to the two targets emerge at 1.231 and 1.252 m, respectively. The distance between the two targets is measured to be 2.1 cm, which is very close to the actual distance. These results can soundly validate the high range resolution of the established MIMO radar.

Then, to verify the super-resolution imaging capability of the proposed photonics-based MIMO radar system in azimuth and elevation directions, 3-D imaging experiments are carried out. The experiment is carried out in an anechoic chamber with the experimental scenario shown in Fig. 6. Specifically, two corner reflectors (size: 2 × 2 × 2 cm) placed approximately ∼4.6 m away from the radar transceiver are employed to simulate a set of ideal point targets. The two reflectors are separated by 0.02 m, 0.03 m (0.3°), and 0.03 m (0.3°) in range direction, azimuth direction, and elevation direction, respectively. As a comparison, the target image is first reconstructed by the traditional DBF method, and the results are shown in Fig. 7. In these figures, the targets are presented in both 2-D and 3-D views, in which the 2-D views are formed by the maximum value projection to the coordinate planes, and the 3-D view is the scatterplot of the points of which the intensity values are larger than 1% of the peak one in the region. As can be seen from Fig. 7, the reconstructed image has a high range resolution thanks to the application of broadband LFM signals. For traditional MIMO radar with the DBF method, the theoretical resolutions in the azimuth and elevation directions are 2° and 2°, which is determined by the baseline length of the MIMO array [34]. The limited azimuth and elevation resolution, which are six times of the target separation, makes it impossible to distinguish the two targets in azimuth and elevation directions. In addition, the imaging results in Fig. 7 are blurred with strong interference, hindering effective identification of the actual scatterers. This is due to the absence of prior information about the targets in the DBF method, leading to inherent challenges such as wide main-lobe width and the presence of high-energy sidelobes. When the proposed DCI method is employed, a random matrix is formed by generating 8 × 8 × 5000 uniformly distributed random phase modulation terms within the range of $[-\pi, \pi]$. Based on this matrix, random phase modulation is implemented to

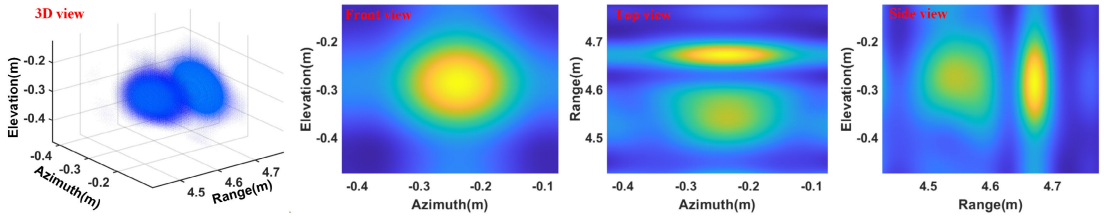

Fig. 10. Reconstructed images of the U-shaped complex target using the DBF method.

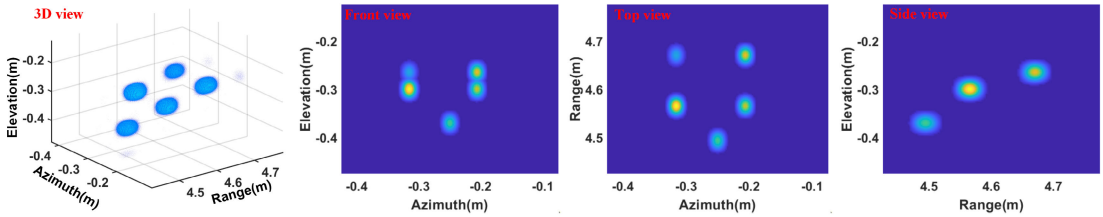

Fig. 11. Reconstructed images of the U-shaped complex target using the proposed DCI method.

the received signals in the digital domain. An imaging area with a size of 0.5 m (range) × 0.5 m (azimuth) × 0.5 m (elevation) is defined around the target, which is divided into 25 (range) × 16 (azimuth) × 16 (elevation) units. This imaging unit size is the minimum to maintain the nonsingularity of the observation matrix, representing the actual resolution capability achievable by the constructed radar system. The orthogonal matching pursuit (OMP) algorithm is adopted as the sparse recovery algorithm to solve the imaging equation of the DCI method because of its simple structure and fast speed. In the imaging results shown in Fig. 8, the two targets are well distinguished in range, azimuth, and elevation directions. Moreover, the amplitudes of the reconstructed targets are much stronger than those from surrounding regions, which means that the corner reflectors are well focused without obvious interference. Therefore, based on the proposed DCI method, the established photonics-based MIMO radar achieves forward-looking imaging with a resolution six times higher than that determined by the Rayleigh limit in both azimuth and elevation directions.

Finally, to imitate real scenes, a complex U-shape target composed of five corner reflectors (size: 5 × 5 × 5 cm) is applied, as shown in Fig. 9. Upon target detection using the established photonics-based MIMO radar, the received signals are processed via the traditional DBF method and the proposed DCI method. The reconstructed 3-D imaging results are depicted in Figs. 10 and 11, respectively. The amplitude of radar echoes differs among reflectors based on the observation angle. Fig. 10 shows that benefitting from the superior range resolution, the traditional DBF method can distinguish the reflectors with strong echoes in the range direction. However, the reflectors with weaker echoes tend to exhibit aliasing. Moreover, owing to the limited azimuth and elevation resolution, there is an overlap among the reflectors, resulting in an inability to discern the shape of the target in these two directions. When the proposed DCI method is applied, from Fig. 11, it is found that the reconstructed images match well with the geometric features of the target. Thanks to the excellent super-resolution imaging capability of the DCI method, each corner reflector can be accurately reconstructed in all three dimensions within the imaging results. Meanwhile, the DCI method overcomes the influence of the large main-lobe width and the presence of high-energy sidelobes, resulting in a well-focused and high-contrast image. Therefore, the imaging results provide robust evidence that the proposed photonics-based broadband MIMO radar can achieve multidimensional high-resolution forward-looking imaging in intricate real-world scenarios.

IV. Conclusion

In conclusion, we have proposed a photonics-based MIMO radar with broadband DCI method and demonstrated its application in high-resolution forward-looking imaging. The radar employs an optical injection semiconductor laser to generate broadband LFM signals in the transmitter and uses photonic frequency mixing for de-chirping the radar echoes. Thanks to the use of microwave photonic technologies, the radar transceivers can be operated with a large bandwidth. Meanwhile, the proposed MIMO radar works in a TDM manner, which allows a high spectral efficiency and a good orthogonality between different channels. Furthermore, by introducing digital phase modulations to the de-chirped signals and solving the constructed imaging equation using the sparse reconstruction method, high-resolution imaging breaking the Rayleigh resolution limit is realized. Through experimental investigation of a photonics-based 8 × 8 MIMO radar with an 8-GHz (18–26 GHz) bandwidth, the feasibility of the established radar system and the advantage of the proposed imaging method are verified.

References

[1] D. A. Ausherman, A. Kozma, J. L. Walker, H. M. Jones, and E. C. Poggio, "Developments in radar imaging," *IEEE Trans. Aerosp. Electron. Syst.*, vol. AES-20, no. 4, pp. 363–400, Jul. 1984.

[2] D. Bleh et al., "W-band time-domain multiplexing FMCW MIMO radar for far-field 3-D imaging," *IEEE Trans. Microw. Theory Techn.*, vol. 65, no. 9, pp. 3474–3484, Sep. 2017.

[3] A. Seeds and K. Williams, "Microwave photonics," *J. Lightw. Technol.*, vol. 24, no. 12, pp. 4628–4641, Dec. 2006.

[4] J. Yao, "Microwave photonics," *J. Lightw. Technol.*, vol. 27, no. 3, pp. 314–335, Feb. 1, 2009.

[5] J. Capmany and D. Novak, "Microwave photonics combines two worlds," *Nature Photon.*, vol. 1, no. 6, pp. 319–330, Jun. 2007.

[6] Y. Zhang, F. Zhang, and S. Pan, "Generation of frequency-multiplied and phase-coded signal using an optical polarization division multiplexing modulator," *IEEE Trans. Microw. Theory Techn.*, vol. 65, no. 2, pp. 651–660, Feb. 2017.

[7] S. S. S. Panda, T. Panigrahi, S. R. Parne, S. L. Sabat, and L. R. Cenkeramaddi, "Recent advances and future directions of microwave photonic radars: A review," *IEEE Sensors J.*, vol. 21, no. 19, pp. 21144–21158, Oct. 2021.

[8] F. Scotti, F. Laghezza, P. Ghelfi, and A. Bogoni, "Multi-band software-defined coherent radar based on a single photonic transceiver," *IEEE Trans. Microw. Theory Techn.*, vol. 63, no. 2, pp. 546–552, Feb. 2015.

[9] S. Maresca et al., "Coherent MIMO radar network enabled by photonics with unprecedented resolution," *Opt. Lett.*, vol. 45, no. 14, p. 3953, 2020.

[10] A. Bogoni et al., "2/3D imaging based on photonics-enabled multi-band MIMO radar system," *Target*, vol. 5, p. 4, May 2020.

[11] J. Yao, "Microwave photonic systems," *J. Lightw. Technol.*, vol. 40, no. 20, pp. 6595–6607, Oct. 15, 2022.

[12] Z. Zhang, Y. Liu, T. Stephens, and B. J. Eggleton, "Photonic radar for contactless vital sign detection," *Nature Photon.*, vol. 17, no. 9, pp. 791–797, Sep. 2023.

[13] R. Li et al., "Demonstration of a microwave photonic synthetic aperture radar based on photonic-assisted signal generation and stretch processing," *Opt. Exp.*, vol. 25, no. 13, pp. 14334–14340, Jun. 2017.

[14] Y. Bae, J. Shin, S.-G. Lee, and H. Kim, "Field experiment of photonic radar for low-RCS target detection and high-resolution image acquisition," *IEEE Access*, vol. 9, pp. 63559–63566, 2021.

[15] F. Zhang et al., "Photonics-based broadband radar for high-resolution and real-time inverse synthetic aperture imaging," *Opt. Exp.*, vol. 25, no. 14, pp. 16274–16281, Jul. 2017.

[16] D. Grodensky, D. Kravitz, and A. Zadok, "Ultra-wideband microwave-photonic noise radar based on optical waveform generation," *IEEE Photon. Technol. Lett.*, vol. 24, no. 10, pp. 839–841, May 2012.

[17] P. Ghelfi et al., "A fully photonics-based coherent radar system," *Nature*, vol. 507, no. 7492, pp. 341–345, Mar. 2014.

[18] W. Zou, H. Zhang, X. Long, S. Zhang, Y. Cui, and J. Chen, "All optical central-frequency-programmable and bandwidth tailorable radar," *Sci. Rep.*, vol. 6, no. 1, Jan. 2016, Art. no. 19786.

[19] S. Peng et al., "High-resolution W-band ISAR imaging system utilizing a logic-operation-based photonic digital-to-analog converter," *Opt. Exp.*, vol. 26, no. 2, pp. 1978–1987, Jan. 2018.

[20] G. Sun, F. Zhang, and S. Pan, "Photonic-assisted high-resolution incoherent back projection synthetic aperture radar imaging," *Opt. Commun.*, vol. 466, Jul. 2020, Art. no. 125633.

[21] G. Sun, F. Zhang, and S. Pan, "Millimeter-level resolution through-the-wall radar imaging enabled by an optically injected semiconductor laser," *Opt. Lett.*, vol. 46, no. 22, p. 5659, Nov. 2021.

[22] C.-C. Chen and H. C. Andrews, "Target-motion-induced radar imaging," *IEEE Trans. Aerosp. Electron. Syst.*, vol. AES-16, no. 1, pp. 2–14, Jan. 1980.

[23] D. E. Wahl, F. H. Eichel, D. C. Ghiglia, and C. V. Jakowatz, "Phase gradient autofocus-a robust tool for high resolution SAR phase correction," *IEEE Trans. Aerosp. Electron. Syst.*, vol. 30, no. 3, pp. 827–835, Jul. 1994.

[24] S.-Y. Jeon et al., "W-band MIMO FMCW radar system with simultaneous transmission of orthogonal waveforms for high-resolution imaging," *IEEE Trans. Microw. Theory Techn.*, vol. 66, no. 11, pp. 5051–5064, Nov. 2018.

[25] L. Xu, J. Li, and P. Stoica, "Radar imaging via adaptive MIMO techniques," in *Proc. 14th Eur. Signal Process. Conf.*, Florence, Italy, Sep. 2006, pp. 1–5.

[26] H. Liu, X. Wang, B. Jiu, J. Yan, M. Wu, and Z. Bao, "Wideband MIMO radar waveform design for multiple target imaging," *IEEE Sensors J.*, vol. 16, no. 23, pp. 8545–8556, Dec. 2016.

[27] S. Sun, A. P. Petropulu, and H. V. Poor, "MIMO radar for advanced driver-assistance systems and autonomous driving: Advantages and challenges," *IEEE Signal Process. Mag.*, vol. 37, no. 4, pp. 98–117, Jul. 2020.

[28] X. Xiao et al., "Photonics-based wideband distributed coherent aperture radar system," *Opt. Exp.*, vol. 26, no. 26, p. 33783, Dec. 2018.

[29] G. Serafino et al., "A photonics-assisted multi-band MIMO radar network for the port of the future," *IEEE J. Sel. Topics Quantum Electron.*, vol. 27, no. 6, pp. 1–13, Nov. 2021.

[30] F. Berland et al., "Microwave photonic MIMO radar for short-range 3D imaging," *IEEE Access*, vol. 8, pp. 107326–107334, 2020.

[31] A. Wang et al., "Microwave photonic radar system with ultra-flexible frequency-domain tunability," *Opt. Exp.*, vol. 29, no. 9, p. 13887, 2021.

[32] B. Gao, F. Zhang, G. Sun, Y. Xiang, and S. Pan, "Microwave photonic MIMO radar for high-resolution imaging," *J. Lightw. Technol.*, vol. 39, no. 24, pp. 7726–7733, Dec. 2021.

[33] F. Zhang, G. Sun, Y. Zhou, B. Gao, and S. Pan, "Towards high-resolution imaging with photonics-based time division multiplexing MIMO radar," *IEEE J. Sel. Topics Quantum Electron.*, vol. 28, no. 5, pp. 1–10, Sep. 2022.

[34] J. Dong et al., "Photonics-enabled distributed MIMO radar for high-resolution 3D imaging," *Photon. Res.*, vol. 10, no. 7, p. 1679, Jul. 2022.

[35] P. Zhou, F. Zhang, Q. Guo, S. Li, and S. Pan, "Reconfigurable radar waveform generation based on an optically injected semiconductor laser," *IEEE J. Sel. Topics Quantum Electron.*, vol. 23, no. 6, pp. 1–9, Nov. 2017.

[36] P. Zhou, F. Zhang, Q. Guo, and S. Pan, "Linearly chirped microwave waveform generation with large time-bandwidth product by optically injected semiconductor laser," *Opt. Exp.*, vol. 24, no. 16, p. 18460, Aug. 2016.

[37] K.-H. Lo, S.-K. Hwang, and S. Donati, "Optical feedback stabilization of photonic microwave generation using period-one nonlinear dynamics of semiconductor lasers," *Opt. Exp.*, vol. 22, no. 15, p. 18648, 2014.

[38] J. S. Suelzer, T. B. Simpson, P. Devgan, and N. G. Usechak, "Tunable low-phase-noise microwave signals from an optically injected semiconductor laser with opto-electronic feedback," *Opt. Lett.*, vol. 42, no. 16, pp. 3181–3184, Aug. 2017.

[39] C. Xue, S. Ji, Y. Hong, N. Jiang, H. Li, and K. Qiu, "Numerical investigation of photonic microwave generation in an optically injected semiconductor laser subject to filtered optical feedback," *Opt. Exp.*, vol. 27, no. 4, p. 5065, 2019.

[40] J.-P. Zhuang, X.-Z. Li, S.-S. Li, and S.-C. Chan, "Frequency-modulated microwave generation with feedback stabilization using an optically injected semiconductor laser," *Opt. Lett.*, vol. 41, no. 24, p. 5764, 2016.

[41] W. Li and J. Yao, "Generation of linearly chirped microwave waveform with an increased time-bandwidth product based on a tunable optoelectronic oscillator and a recirculating phase modulation loop," *J. Lightw. Technol.*, vol. 32, no. 20, pp. 3573–3579, Oct. 2014.

[42] X. Lin et al., "Frequency-modulated continuous-wave generation based on an optically injected semiconductor laser with optical feedback stabilization," *Opt. Exp.*, vol. 27, no. 2, p. 1217, 2019.

[43] B. Zhang, D. Zhu, P. Zhou, C. Xie, and S. Pan, "Tunable triangular frequency modulated microwave waveform generation with improved linearity using an optically injected semiconductor laser," *Appl. Opt.*, vol. 58, no. 20, p. 5479, Jul. 2019.

[44] R. Li et al., "PFDIR—A wideband photonic-assisted SAR system," *IEEE Trans. Aerosp. Electron. Syst.*, vol. 59, no. 4, pp. 4333–4346, Aug. 2023.

[45] J. Ding, M. Wang, H. Kang, and Z. Wang, "MIMO radar super-resolution imaging based on reconstruction of the measurement matrix of compressed sensing," *IEEE Geosci. Remote Sens. Lett.*, vol. 19, pp. 1–5, 2022.

[46] L. Kang, Y. Luo, Q. Zhang, X.-W. Liu, and B.-S. Liang, "3-D scattering image sparse reconstruction via radar network," *IEEE Trans. Geosci. Remote Sens.*, vol. 60, 2022, Art. no. 5100414.

[47] M. Schurwanz, J. Mietzner, M. De Muirier, T. Tiedemann, and P. Adam Hoeher, "Compressed sensing-based obstacle detection for future urban air mobility scenarios," *IEEE Sensors Lett.*, vol. 7, no. 11, pp. 1–4, Nov. 2023.

[48] Q. Cheng, A. Alomainy, and Y. Hao, "Near-field millimeter-wave phased array imaging with compressive sensing," *IEEE Access*, vol. 5, pp. 18975–18986, 2017.